2008

Feasibility testing for SalSA neutrino astrophysics project

Jarrod Christopher Marsh
Louisiana State University and Agricultural and Mechanical College, jcm177@msstate.edu

FEASIBILITY TESTING FOR SALSA NEUTRINO ASTROPHYSICS PROJECT

A Thesis
Submitted to the Graduate Faculty of the
Louisiana State University and
Agricultural and Mechanical College
in partial fulfillment of the
requirements for the degree of
Master of Science

in

The Department of Physics & Astronomy

by
Jarrod Marsh
B.S. Louisiana State University, 2005
May 2008

TABLE OF CONTENTS

LIST OF FIGURES

ABSTRACT

Research is presented that was performed to determine possible locations for a full scale Salt Dome Shower Array (SalSA) neutrino telescope sensitive to energies from TeV (10^{12} eV), PeV (10^{15} eV), and EeV (10^{18} eV) neutrinos. A detector to test possible site locations was designed around a half-Watt Ham radio to transmit short pulses of 145.500 MHz radiation. The research began by designing the system. Several phases of design took place as the system was refined and calibrated. Once finished, it was taken into a field and tested. The objective was to determine how the signals depended on distance. In principle, there should have been a linear relationship between distance and voltage. After successful testing, the system will be taken to a salt mine to accurately determine the index of refraction and attenuation length of that particular mine's salt.

1. BACKGROUND

1.1 Introduction

Over the past few decades the astronomical community has become increasingly interested in the subject of particle astrophysics. Years of observations have confirmed that the universe is innundated with highly energetic atomic nuclei collectively known as cosmic rays. These particles are believed to arrive from the most energetic structures in the universe and carry information about the processes driving these structures. In response, the scientific community has constructed and operated massive facilities such as Fly's Eye and Auger in attempts to detect and measure high energy cosmic rays. The science is limited by two considerations: 1) cosmic rays are charged so that all but the highest energy ($> 10^{19}$ eV) particles will be deflected by the galactic magnetic fields and 2) cosmic rays with sufficient energy to avoid deflection will be attenuated over long distances by the well known Greisen-Zatsepin-Kuz'min (GZK) effect. These considerations limit the ability to determine the actual sources of the cosmic rays.

Recently particle astrophysics has begun to look for a different particle: the neutrino. Neutrinos are produced in the same nuclear reactions that produce cosmic rays, so they carry the same information about the regions of the universe where the cosmic rays were formed. Neutrinos are uncharged, therefore are not deflected by magnetic fields, and because they only interact via the weak force they are immune to almost all attenuation. A neutrino that reaches Earth came directly from its point of origin and so can, in principle, be used to determine the location of the source.

Neutrinos, however, present their own set of difficulties. First and foremost is the issue of actually detecting them. Since neutrinos only interact weakly they travel to Earth untouched, but the same interaction property also makes them extremely difficult to catch upon their arrival. Detecting these neutrinos requires very large detector volumes (e.g 50,000 gallons of water in the case of Super Kamiokande, and over a cubic kilometer of ice for IceCube). At higher energies the neutrino interaction cross section increases, but the neutrinos are so rare that obtaining a high enough event rate requires detectors with detector surface areas in the square kilometer range. As

a result, detectors for Ultra High Energy (UHE) neutrinos are expensive, resource-consuming, and often must be constructed in extremely challenging areas. An alternative is SalSA. As its name implies, SalSA will be built in a pre-dug salt mine at minimal cost and risk. This paper covers the design, construction, and testing of equipment built to measure important properties of salt in various mines to determine which would be the best location for an initial SalSA test and possibly for a full scale telescope.

1.2 Neutrino Sources

Extraterrestrial neutrinos are classified into catagories based on their energy: Solar neutrinos, High Energy (HE) neutrinos, and Ultra High Energy (UHE) neutrinos. This paper will be limited to HE and UHE neutrino sources.

1.2.1 HE Neutrinos

One source of neutrinos are the accretion disks that form around black holes and neutron stars. In this case, cosmic ray protons interact with nucleons in the disk, creating neutrinos and gamma rays.

$$\mathrm{p} + \mathrm{N} \rightarrow \text{hadrons} + \pi^0 + \pi^{\pm}$$

The pions will then decay through

$$\pi^+ \rightarrow \nu_\mu + \mu^+ \rightarrow \nu_\mu + \overline{\nu_\mu} + \nu_e + e^+, \tag{1.1}$$

$$\pi^- \rightarrow \overline{\nu_\mu} + \mu^- \rightarrow \overline{\nu_\mu} + \nu_\mu + \overline{\nu_e} + e^- \tag{1.2}$$

and

$$\pi^0 \rightarrow 2\gamma. \tag{1.3}$$

Accelerated protons can impact either the surface of a neutron star or the gas and dust in the disk at extremely high energy, producing neutrinos and gamma rays. The gamma rays may not make it out of the disk due to interactions and attenuation with the disk material, but neutrinos below ~ 100 TeV may pass right through and carry information about the astrophysical processes occuring at the source.[21]

Other sources that could display similar particle interactions are sources behind dust clouds, sources surrounded by matter, sources too far away for cosmic rays to propagate, and some exotic sources such as dark matter.[21] It should be possible to predict the measured UHE neutrino flux based on the observed UHE gamma rays. The pion decay chain above indicates that for every three neutrinos (and every three antineutrinos) produced there are two corresponding gamma rays. Therefore an observer located immediately adjacent to the production process would observe a three to one ratio of neutrinos and antineutrinos to gamma rays. However, gamma rays are highly attenuated by the material surrounding the production sites so that the neutrino/antineutrino flux may in fact be large compared to the flux of energetic gamma rays. The scaling between the gamma ray and neutrino intensities may be written as

$$\frac{dS_\nu}{dE} \sim 0.3\lambda(E)\frac{dS_\gamma}{dE} \tag{1.4}$$

where $\frac{dS_i}{dE}$ denotes the energy dependent spectra of the particles, $\lambda(E)$ is the scaling factor, and the 0.3 comes from relative detection probabilities scaled to actual proposed detectors.[4]

1.2.2 Cosmic Rays & UHE Neutrinos

Cosmic rays are completely ionized nuclei that have been accelerated to extremely relativistic velocities. Most cosmic rays are single protons, yet there are significant amounts of iron, α particles, and others. At high energies, the measured percentages are 50% protons, 25% α particles, 13% CNO, and 13% iron.[20] As has been stated, cosmic rays are deflected by magnetic fields. A simple calculation will demonstrate just how much of an effect the galatic magnetic field alone will have on a cosmic ray. The deflection radius in centimeters is given by

$$R_L = \frac{E}{300ZB} \quad [20]. \tag{1.5}$$

E is the particle energy in eV, B is the magnetic field strength in Gauss, and Z is the particle's charge. Given a particle of energy $E = 10^{17}$ eV, a galactic magnetic field of a few microgauss ($\sim 10^{-6}$ Gauss), and that the particle is a proton ($Z = 1$ Coulomb), $R_L = 3 \cdot 10^{20}$ cm, much less than a galactic diameter. This shows that even the relatively weak field of the galaxy can induce significant deflection in high energy particles.

The potential sources of cosmic rays include solar and stellar flares, stellar winds, shocks and jets produced by pulsars, black holes, supernovae, and Active Galactic Nuclei (AGNs). The only sources sufficiently large and with sufficiently strong magnetic fields to accelerate particles to $> 10^{20}$ eV energies are extragalactic AGN. If cosmic rays are accelerated in extragalactic sources to energies in excess of 10^{20} eV, though, they will interact with the cosmic

microwave background (CMB) photons and decay into pions as they propagate to Earth. These proton-photon interactions will cause the cosmic rays to lost $\sim 20\%$ of their energy in each collision.[27] As a result, UHE cosmic rays do not propagate beyond ~ 6 megaparsecs, and one expects a steepening in the UHE cosmic ray spectrum. This is the GZK limit.[13]

Zatsepin and Kuz'min define the proton-photon interaction time as

$$\tau_{p\gamma} = \frac{2\pi^2 c^2 \hbar^3 \gamma^2}{k_B T \phi} \tag{1.6}$$

where $\gamma = \frac{E_p}{M_p c^2}$ and ϕ is the energy dependent cosmic ray flux. The total absorption cross section for the cosmic ray protons on the CMB photons, $\sigma_{p\gamma}(E)$ (also know as the photoproduction cross section for π^0 and $\pi^{\pm}$ mesons), is assumed to be constant above energies of 1 TeV.[27] Assigning $\sigma_{p\gamma}$ a value of 10^{-28}cm^2 (1 barn) allows $\tau_{p\gamma}$ to be determined at various energies. Zatsepin and Kuz'min calculate that at energies just below 10^{20}eV, the interaction time decreases rapidly to about 10^{15} seconds (10^8 years) because of the increasing center of mass energy of the proton-photon system. This is two orders of magnitude less than the 10^{10} years of the estimated age of the universe and shows quite clearly that there will be a cutoff in the cosmic ray spectrum above 10^{20}eV. The most recent results from Auger show this cutoff.[5]

A useful check is to calculate the mean free path of a cosmic ray proton. Mean free path is defined as $\lambda = \frac{1}{n\sigma}$. Assuming the photon density, n, is 550 cm^{-3}[13] and using the value of $\sigma_{p\gamma}$ from Zatsepin and Kuz'min, the mean free path is of order 6000 kpc. The nearest known candidate for UHE cosmic rays is the active galactic nucleus in Centaurus A, a distance of 4.7 Mpc.[2] This is close enough that some cosmic rays should be seen but far enough away to significantly reduce the flux. In fact, the most recent results from the Pierre Auger Observatory have correlated the UHE cosmic ray flux with AGNs and have identified Cen A as a potential source[5]

The mechanics of the GZK effect are actually rather simple. The cosmic ray proton interacts with a photon via

$$\gamma + p \rightarrow \Delta^*(1232) \rightarrow \begin{array}{l} n + \pi^+ \\ p + \pi^0 \end{array} \tag{1.7}$$

The pions decay in the same manner as Equations 1.1 and 1.3. This process guarantees three neutrinos for every π^+ produced from the GZK effect. Since the GZK effect has been shown to occur, the presence of UHE cosmic rays virtually guarantees the presence of UHE neutrinos. With the most recent AUGER results clearly demonstrating

that both UHE cosmic rays and the GZK cutoff do indeed exist, the search for the corresponding neutrinos takes on a new importance.

1.3 Ultra-High Energy Detectors

1.3.1 Deep Ocean Experiments

As the study of solar neutrinos developed, many astronomers began to wonder if higher energy neutrinos from other sources could be measured. The neutrinos produced by the sun, while extremely informative, only carry energies of a few MeV. Since the energy of produced particles scales with the energy of the originating event, it seemed reasonable that higher energy events would produce correspondingly higher energy neutrinos. The problem was that detectors for larger energies required larger target masses because the flux is so low. If the lowest energy solar neutrinos required a detector filled with 100,000 gallons of perchloroethelyne, what would be required to detect neutrinos from the highest energy sources?

The beginning of the answer came in the late 1970s to early 1980s. The required detector size was massive, on the order of millions of tons of material and thousands of square meters of surface area. Unlike solar neutrinos, UHE neutrinos have much larger cross sections. This means they will interact more readily than lower energy neutrinos. However, there are far fewer sources of UHE neutrinos and the distances to extragalactic sources are large. Fortunately, with a large enough transparent medium UHE neutrinos could be detected.

The first true experimental attempt began in 1976 at the Deep Underwater Muon and Neutrino Detection (DUMAND) Project. DUMAND was proposed to be a series of underwater "strings" carrying photomultiplier tubes (PMTs) submerged in the Pacific Ocean near Keyhole Point on Big Island, Hawaii. The entire detector was to cover an area of 20,000 m^2.[7] Neutrino interactions produce seconday muons, which in turn generate optical Čerênkov radiation in the transparent ocean water. The PMTs would detect the characteristic blue Čerênkov photons produced by the secondary muons. The problem was that muons were not produced solely by neutrino interactions. They could be produced by cosmic rays in the upper atmosphere as well. The cosmic ray muons could completely drown out those produced by neutrinos. The solution: only look for upward moving events. In the range of 10^{18} eV most neutrinos will interact while passing through the earth. Some, however, will pass through the entire diameter of the earth and then interact in the last few meters of rock. This will produce an upward moving muon shower. When the shower reaches the ocean water, there will be a pulse of Čerênkov light. In 1993, DUMAND managed to submerge a test string carrying seven optical modules to a depth of 4800 meters. The communication/power cable functioned, but unfortunately many of the systems on the string itself shorted out. Two years later the US Department of Energy cancelled funding on the project.[24]

Despite the setbacks with DUMAND, the UHE neutrino field continued to progress. A direct decendent of DUMAND is the Neutrino Extended Submarine Telescope with Oceanographic Research (NESTOR). NESTOR is a branch of the National Observatory of Athens in Greece. The telescope is located about fourteen miles off the Peloponnesian peninsula, near the town of Pylos. The site was chosen for its access to the sea and proximity to a sheltered harbor. The extreme depth in that region of the Mediterranean is ideal for shielding the telescope from cosmic ray muons.[25]

NESTOR is comprised of underwater towers. Each of the twelve levels of the towers are thirty-two meter diameter six-arm stars with PMTs at the corners. There is a twenty meter clearance between levels. In total, each tower carries 168 PMTs. The system is designed to work in much the same manner as DUMAND, the difference being that where DUMAND's detectors were all downward facing, NESTOR will have half facing upwards. This gives NESTOR a 4π viewing angle, yet because NESTOR is located 4000 meters underwater the muon background is still highly attenuated.[19] NESTOR's long-term goals are to deploy seven of these towers. Six of them are to be located in a hexagon surrounding a central tower. The total estimated viewing area will be greater than $3{\cdot}10^5$ square meters. The completed array will allow NESTOR to measure neutrinos with energies up to the PeV range.[19] In 2003, a single NESTOR tower was deployed for instrument testing purposes. The tower performed so well that the NESTOR team was able to make background measurements of the cosmic ray spectrum and identify and reject bioluminesent sources of inteference. The team is currently planning the next stages of detector construction.[10]

The Astronomy with a Neutrino Telescope and Abyss environmental RESearch (ANTARES) project is another deep ocean neutrino telescope. ANTARES is located off the coast of Marseilles, France. As with the other detectors, it is built of long strings containing PMTs. ANTARES' strings are 350 meters long with sixteen platforms for detector mounting.[23] There are to be a total of ten strings submerged to a depth of 2000 meters. ANTARES has been experiencing difficulties due to pollution from large cities on the coast of France. Upward facing detectors were rejected due to silt buildup on the glass housings. Because it only uses downward facing PMTs, it receives no downward travelling flux. Despite these issues, the last of the five initial strings were installed at the ANTARES site on January 29, 2007, and by the end of the day were taking preliminary data.[23]

1.3.2 Ice Experiments

Sea water has an estimated attenuation length around 50 meters for blue light. The ANTARES collaboration measured attenuation lengths of 48-61 meters at a wavelength of 466 nm. NESTOR found attenuation lengths of 55 meters. Silt is the primary cause. Other factors such as industrial and civil pollution combined with aquatic organisms attaching themselves to the PMTs also limit the distance signals travel. Working at these depths in the

ocean also creates serious safety, financial, and logistical issues. NESTOR and ANTARES are both designed to be as automatic and remote controlled as possible to minimize the need for manned underwater excursions, but the trade off is an increase in cost and technical capabilities.

To avoid these problems, newer detectors are using Antarctic ice as a target medium. The logistical advantages are immediately apparent. First, there is no need to put crews and equipment at risk by sending them to extreme depths. Second, the complexity of the equipment decreases greatly once there is no need to submerge it in conductive sea water. Antarctic ice also has a predicted attenuation length of 85-255 meters, several times greater than that of sea water meaning detectors can be more spread out than in the ocean.[6]

Several telescopes have been designed and built in the Antarctic using the ice at the geographic south pole. The Antarctic Muon and Neutrino Detector Array (AMANDA) is a series of detector strings embedded over 2000 meters deep in the ice at the South Pole. The nineteen strings are arranged into a cylinder about 120 meters wide. The drawback is that once the strings are frozen in place, they cannot be removed for repair and maintenance.[22] In 2003 AMANDA was able to place upper limits on the UHE neutrino flux. They quoted an upper limit of $8.4 \cdot 10^{-7} \frac{\text{GeV}}{\text{cm}^2 \text{ sec sr}}$ on the E^{-2} spectrum over a range of 6 TeV to 1 PeV.[9]

After running for several years, the AMANDA experiment was reorganized as the IceCube experiment. IceCube picks up where AMANDA left off. The technology is essentially unchanged from the original AMANDA design. The difference is primarily the scale of the project. While the largest version of AMANDA (AMANDA-II) had 19 strings, IceCube will have 80 strings, each carrying 60 optical modules and buried in the ice at a depth of 2400 meters. IceCube will have a target volume on the order of a cubic kilometer and be capable of seeing neutrinos ranging in energy up to > 1 PeV.[11, 14]

The Radio Ice Čerênkov Experiment (RICE) is a new type of neutrino telescope being constructed near AMANDA/ IceCube. As its name implies, RICE looks for radio signals. These signals are a specific form of Čerênkov radiation first proposed by Soviet physicist Gurgen Askaryan in 1962. In the right medium, a particle shower produced by a neutrino will create a brief but intensely powerful pulse of radio waves. Radio detection of UHE neutrinos has several advantages over previous optical methods. First, the earth is fairly opaque to neutrinos at the energies RICE will observe (> 1 PeV) so there will be very few events moving up from below the detector. At UHE energies, RICE expects the signal to be dominated by neutrinos, so cosmic ray muons are not a problem.[8] Second, radio signals have a much longer wavelength than optical light. The signals produced from the Askaryan Effect will not be attenuated as much as optical photons by dust and air bubbles trapped in the ice. AMANDA and IceCube have both reported problems with signals being scattered after only a few meters of propagation.[19] RICE does not have this problem.

1.4 Radio Measurements in SalSA

1.4.1 Askaryan Effect

The Askaryan effect is related to the better known Čerênkov effect. The difference is that the Askaryan effect is the result of a shower of charged particles travelling through a dense, radiotransparent medium such as ice or rock salt. As the shower progresses, the wave fronts of each of the particles coherently stacks producing a very short, but very powerful burst of radio (RF) signal. Askaryan proposed in 1962 that the effect could be used to detect and measure UHE neutrinos; however, it is only in recent years that detector technology has become sufficiently advanced.[18] To date, the Askaryan effect has been observed in silica sand, Antarctic ice, and salt.[12, 18]

To completely understand the Askaryan effect it is necessary to start from Čerênkov Radiation. Čerênkov Radiation is the result of a charged particle moving faster than the phase velocity of electromagnetic fields in a dielectric, i.e., $v > \frac{c}{\sqrt{\epsilon(\omega)}}$ where v is the speed of the particle, $\epsilon(\omega)$ is the frequency dependent dielectric constant, and c is the vacuum speed of light. This allows one to write (in Gaussian units) the energy radiated per distance travelled as

$$\left(\frac{dE}{dx}\right)_{rad} = \frac{(Ze)^2}{c^2}\int_{\epsilon(\omega)>(1/\beta^2)} \omega\left(1 - \frac{1}{\beta^2\epsilon(\omega)}\right)d\omega. \tag{1.8}$$

This equation was first published by Frank and Tamm in 1937, three years after Čerênkov published his discovery of this particular form of radiation.[15]

Next, define an angle θ_c that is the angle between the particle's direction of travel and the vector normal to the radiation front. This angle can be written as the ratio of the parallel (E_1) and transverse (E_2) components of the electric field, with respect to the particle's velocity vector.

$$\tan\theta_c = -\frac{E_1}{E_2} \tag{1.9}$$

E_1 and E_2 are defined at an observation point a as $E_1 = -\frac{\imath Ze\omega}{v^2}\sqrt{\frac{2}{\pi}}\left[\frac{1}{\epsilon(\omega)} - \beta^2\right]K_0(\lambda a)$ and $E_2 = \frac{Ze}{v}\sqrt{\frac{2}{\pi}}\frac{\lambda}{\epsilon(\omega)}K_1(\lambda a)$ where the $K_n(x)$ are the modified Bessel functions. In the far field ($\lambda a \gg 1$) the components of the electric field become $E_1 = i\frac{Ze\omega}{c^2}\left[1 - \frac{1}{\beta^2\epsilon(\omega)}\right]\frac{e^{-\lambda a}}{\sqrt{\lambda a}}$ and $E_2 = \frac{Ze}{\nu\epsilon(\omega)}\sqrt{\frac{\lambda}{a}}e^{-\lambda a}$ respectively. Equation 1.9 then reduces to

$$\cos\theta_c = \frac{1}{\beta\sqrt{\epsilon(\omega)}} \tag{1.10}$$

and allows the condition for Čerênkov radiation ($v > \frac{c}{\sqrt{\epsilon(\omega)}}$) to be expressed as $\cos\theta_c < 1$ where θ_c is a real angle.[15]

What these expressions define is a cone of light analagous to the shock wave produced by supersonic aircraft. The particle is at the apex of the cone, and the slope of the sides is determined by θ_c. This can be quantitatively written by Fourier transforming the frequency dependent vector potential and setting the dielectric term to be independent of frequency.

$$\mathbf{A}(\vec{x},t) = \boldsymbol{\beta}\frac{2Ze}{\sqrt{(x-vt)^2 - (\beta^2\epsilon - 1)\rho^2}} \quad [15] \tag{1.11}$$

where ρ is coordinate of the transverse electric field.

The Askaryan effect is derived from Čerênkov radiation. When a high energy particle, such as a muon, enters a dielectric medium it generates a shower of charged secondary particles. There are two main types of showers: electromagnetic and hadronic. For a discussion of the Askaryan effect, it is useful to limit the discussion to electromagnetic showers since that is what experiments like RICE and SalSA look for. In an electromagnetic shower, the vast majority of the secondaries are positrons, electrons, and photons. The shower begins as an electron or photon enters a dielectric medium. If the primary particle is an electron, the deceleration upon hitting the target will produce photons via the process of bremstrahlung radiation. These secondary photons will decay through pair production into positrons and electrons, which will in turn radiate more photons. So long as the secondary particles remain above a certain cutoff energy, E_c, the process will continue. When the secondaries reach the cutoff energy, the shower will die out. This indicates that as the shower progresses further into the medium, it will increase in width until the average shower particle energy reaches the cutoff, and then rapidly dies away.[17] The charged secondaries generated in the shower will also radiate Čerênkov photons if they exceed the Čerênkov velocity.

The Askaryan effect occurs when there is a charge imbalance between the positrons and electrons generated in the shower. According to the shower mechanics described above, there should be an equal number of electrons and positrons. Experiments show that this is not necessarily the case. Askaryan cites two processes as responsible for the excess electrons: positron annihilation and the dragging of δ and Compton electrons.[1] He began by defining the average production rates of positrons and electrons as

$$\dot{n}_- \quad = \quad \Phi(t) - \frac{n_-}{\tau_-} + \dot{n}_{\delta,C} \tag{1.12}$$

$$\dot{n}_+ \quad = \quad \Phi(t) - \frac{n_+}{\tau_+} \tag{1.13}$$

where $n_\pm$ is the average number of positrons and electrons, $n_{\delta,C}$ is the number of electrons from the Compton and δ electrons, Φ is a generating function of positrons and electrons from pair production, and $\tau_\pm$ is the average lifetime of the respective particles before losing energy to radiation. Note that the n_- equation already has an extra term $(n_{\delta,C})$. Next, write $\frac{1}{\tau_+}$ as $\frac{1}{\tau_-} + \frac{1}{\tau_a}$ where τ_a is defined as the lifetime of the positron before annihilation. Inserting this into Equation 1.13 gives

$$\dot{n}_+ = \Phi(t) - n\left(\frac{1}{\tau_-} + \frac{1}{\tau_a}\right). \tag{1.14}$$

Defining $v = n_- - n_+$ and subtracting Equation 1.14 from Equation 1.12 yields

$$\dot{v} + \frac{v}{\tau_-} = \frac{n_+}{\tau_a} + \dot{n}_{\delta,C}. \tag{1.15}$$

Then set $\frac{n_+}{\tau_a} \approx Ce^{-t/T_+}$, where T_+ is the build up time for the annihilating positrons, and place it into the expression for $\dot{v}$. This gives $v \approx \frac{n_+}{\tau_a\left(\frac{1}{T_+}+\frac{1}{\tau_-}\right)}$ for $t \gg \tau_-$. If $T_+ \sim \tau_-$, then $v \sim \frac{n_+\tau}{\tau_a}$. Defining $\tau \sim \frac{l_{rad}}{c}$ and $\tau_a \sim \frac{1}{N_e\sigma_a c}$ together with the radiation length $l_{rad} = \frac{137}{4ZN_e r_0^2 \ln\left(\frac{183}{Z^{1/3}}\right)}$ allows the construction of the excess charge ratio

$$\frac{\tau}{\tau_a} \approx \frac{137}{4Z}\left(\frac{mc^2}{E_+}\right)\frac{\ln(2E/mc^2)}{\ln(138/Z^{1/3})}.[1] \tag{1.16}$$

where E_+ is the positron energy. For an initial energy of 10^{20} eV, the ratio $\frac{\tau}{\tau_a}$ becomes 0.25, indicating that the number of electrons exceeds the number of positrons by 25%.

Moving charges exceeding the Čerênkov velocity will produce photons. In the case of excess charge, radio frequencies specifically are produced as the Čerênkov light from the negatively charged shower front coherently stacks and the superposition of each electron's Čerênkov signal produces radio frequencies at wavelengths on the order of the width of the shower. This selects specific frequencies, the range of which is determined by the density of the medium. In air, the expected wavelength for coherent emission is on the order of several hundred meters. However, in a dense material such as ice, salt, or even the lunar regolith, the wavelength for coherent emission is on the order of a few centimeters to a few meters, making dense media preferable to air. At UHE energies the expected power of such a signal is about 30 Watts.[1, 8]

1.4.2 Proof of Principle

Testing of the Askaryan Effect was performed in June 2002 at the Stanford Linear Accelerator. This experiment demonstrated that not only was the Askaryan Effect real, but it was perfectly capable of being accurately measured in both energy and direction, quantities critical to the operation of SalSA. The test (designated SLAC T406) used four metric tons of commercial grade salt obtained from the Morton Salt Company. The bricks were arranged in a rectangular block with sides of 116 cm, 200 cm, and 84 cm. Each brick weighed 1.8 kg with a density of 2.08 g/cm^3, slightly less than rock salt. The gamma rays were produced by bombarding aluminum bremsstrahlung targets with an electron beam. The entire array was turned 10° to the SLAC beam line to prevent total internal refraction of the incident gamma rays. Radio detection was primarily accomplished with a three by seven array of etched printed circuit board bowtie antennae placed 10 cm above where the beam line entered the block. A fixed directional horn antenna and a moveable dipole antenna were placed outside the block for further measurements.[12]

One of the more important aspects of this test was to obtain a rough estimate of the attenuation length of an RF signal in salt. The attenuation length is defined as the inverse of the absorption coefficient α ($L_\alpha = \frac{1}{\alpha}$) where

$$\alpha \simeq \frac{2\pi\nu}{c}\sqrt{\epsilon}\,\tan\delta. \tag{1.17}$$

ν is the frequency of the signal, c is the speed of light, ϵ is the real dielectric permittivity, and $\tan\delta$ is the loss coefficient. Choosing ν to be in the VHF range ($\sim$ 150 MHz), ϵ to be 5.9, and $\tan\delta$ experimentally measured as $\leq 10^{-4}$ gives an estimate for α of $7.97 \cdot 10^{-5}$ m^{-1}. This means that $L_\alpha \approx 1300$ m. According to this calculation, signal attenuation should not be noticeable on length scales of a few hundred meters. Although there was not enough salt to perform a proper test of the attenuation length, the experimenters reported that there was no noticeable attenuation over the 0.3-0.4 meter length of their experiment.[12]

To have a standard for comparing results, the electromagnetic shower was simulated using the Electron Gamma Shower 4 (EGS4) code. The limitations of the code prevent it from directly simulating the radio emissions, but it can provide information about the dimensions of the shower and the particle content, including the Askaryan excess electrons. In fact, the code was easily able to create the 25% electron excess expected in the Askaryan effect. One of the first confirmations of the accuracy of the simulations was the physical dimensions of the shower. After the experiment, it was noticed that the shower left a discoloration several centimeters wide at its exit point. The mark corresponds to the position of the core of the shower and is of the same size as the shower core generated by the simulations.[12]

There were three categories of interest: coherence and field strength, polarization and charge tracking, and transition radiation. Coherence is a measure of how the power of the signal varies with shower energy. If the relationship is predictable, then the initial shower energy can be determined by the strength of the RF pulse. Power should increase as the square of the shower energy. The team's measurements clearly demonstrated this behavior.[12]

Measuring the field strength involves the dimensions of the antenna used, the angle of incidence between the signal and the antenna's detection plane, and most importantly, the distance between the antenna and the signal source. For this experiment, the signal was in the far field, allowing the use of several approximations to reduce the complexity of the math. In the far field, the expression for the maximum allowable frequency is

$$f \leq \frac{Rc}{L^2 \cos^2 \theta}. \tag{1.18}$$

where R is the distance between the antenna and source, L is the largest antenna dimension, and θ is the angle of incidence. The bowtie antennae had dimensions of 20 cm at an angle of 25° to the source 38 cm away, corresponding to a maximum allowable frequency of ∼2 GHz. One interesting effect of the far field/near field geometries is that while the shower is in the antenna's far field, the antenna is not in the shower's far field. The shower is continuously generating RF photons as it travels through the media. As the shower passes a particular antenna, it moves from the far field to the near field, changing the frequency response. With an array of antennae, the shower progression can be mapped from the changing frequency responses from the antennae.[12]

The polarization is important because it is expected to be aligned with the direction of shower propagation. Accurate measurement of the polarization could be used to reconstruct the initial particle's path and origin on the sky. This information can also work as a rejection scheme between upward and downward travelling neutrinos. The bowtie antennae used at SLAC were capable of measuring two perpendicular modes of polarization. Due to their geometry, however, there was a 15% crossover rate between signals of orthogonal polarization. To differentiate between the two, the two induced polarized potentials were modeled as

$$V_0 = \mathbf{E} \cdot [\mathbf{h}_0 + \alpha \mathbf{h}_{90}] \tag{1.19}$$

$$V_{90} = \mathbf{E} \cdot [\mathbf{h}_{90} + \alpha \mathbf{h}_0] \tag{1.20}$$

where $\mathbf{h}_{0,90}$ are the orthogonal vector magnitudes of the antennae, and $\mathbf{E}$ is the electric field vector for the shower. Because the induced potentials have a sinusoidal dependence on the angle between the shower and the antenna plane and the antennae are indentical, Equations 1.19 and 1.20 become

$$\begin{aligned} V_0 &= Eh\left[\cos\Psi + \alpha\sin\Psi\right] && (1.21)\\ V_{90} &= Eh\left[\sin\Psi + \alpha\cos\Psi\right] && (1.22)\\ h &\equiv \frac{1}{2}\left(|\mathbf{h}_0| + |\mathbf{h}_{90}|\right) \end{aligned}$$

Because one of the polarized modes was along the beam axis, $\alpha \approx \left(\frac{V_{90}}{V_0}\right)_{on-axis}$. This yields the interface angle as

$$\Psi = -\arctan\left(\frac{\alpha - V_{90}/V_0}{\alpha V_{90}/V_0 - 1}\right). \quad (1.23)$$

Equation 1.23 now relates the angle of polarization projected onto the plane of the antenna to the orthogonally polarized potentials, allowing accurate measurement of polarization leakage and signal reconstruction.

Another effect measured at SLAC was the transition radiation. Transition radiation from the Askaryan charge excess is guaranteed to occur whenever the shower passes into a medium with a significantly different dielectric constant. If the shower were generated in the rock surrounding a salt dome, the transition from rock to salt would produce transition radiation in the forward direction. The ability to detect and measure this radiation would greatly increase the ability of an Askaryan detector to function. This test was not performed using the salt block. Instead, a lead brick and an aluminum brick were used. A significant TR signal was detected indicating that the Askaryan charge excess does indeed produce transition radiation.[12]

1.4.3 SalSA Concept

The approach to be used by SalSA is similar to RICE. The major differences are that SalSA will use rock salt as a target mass instead of ice and that instead of boring vertical shafts for the detectors, SalSA will be laid out horizontally in mine tunnels. The original proposal was to bore several hundred holes into the top of a salt dome and bury strings of detectors similar to those used by RICE. Salt was chosen because naturally occuring salt domes are often greater than 99% pure halide. More importantly, salt is very transparent to radio frequencies. Also, salt domes are much more accessible than Antarctic ice, which greatly reduces the logistical nightmares associated with ICECUBE and RICE.

Each of the SalSA strings was to carry twelve detector nodes. The nodes would have a combination of six

vertically and horizontally polarized antennae for a total of twelve on each. Based on the findings of Stewart and Unterberger, the strings were to have been placed about 250 meters apart. An event trigger would occur when five nodes activated simultaneously.[18] This design would have called for several hundred bore holes. However, the cost of drilling to the required depths has increased recently and is now in excess of $1,000,000 per hole. The concept was then modified so that SalSA would be constructed in a salt mine. A flat array of directional detectors would be laid out along several layers of the mine. This had the advantage of being much cheaper than drilling into new salt, but came at the cost of decreased sensitivity and position resolution.

SalSA is naturally suited for deployment in Louisiana. The Louisiana Gulf Coast is the site of several large and active salt mines, most notably the Avery Island Salt Mine and the Cote Blanche Salt Mine, both located south of New Iberia, LA. The salt in Avery Island has been measured as 98.7% NaCl and 1.2% $CaSO_4$. Radio measurements made in Cote Blanche in the 1970s indicate attenuation lengths of 330 meters at a frequency of 440 MHz. Louisiana is also a good location due to the proximity of the two primary site candidates to one of the major collaborators. Avery Island and Cote Blanche are within 100 miles of the Louisiana State University campus, making Louisiana State University an excellent staging and proving ground for experimental ventures and equipment. Finally, both of the site candidates' management have shown great interest in hosting the experiments at their facilities, allowing research teams to concentrate on their work instead of spending time sorting out safety, power, and other requirements.[3]

2. TECHNICAL DESCRIPTION

2.1 General Overview

The index of refraction of salt can be determined by sending a radio (RF) pulse through the salt and measuring the time it takes to arrive. This approach used what is known as a tone burst system. The system transmits a short burst of RF at a fixed frequency. Simultaneously, a timing signal is sent along a transmission line to the receiver. The difference in arrival times gives the local speed of light and, as a result, the index of refraction.

To determine the attenuation length, the video gate that generates the pulses is removed, leaving a continuous tone. Measuring the voltage on the receiving end as a function of distance gives the attenuation length. Since there is no power restriction due to the gate, the transmitter can be run at its full 5 Watt power setting, allowing for much farther distance measurements out to several attenuation lengths.

2.2 System Components and In-Lab Testing

Figure 2.1 gives a system level look at how this approach works. Each cable is labeled with symbols for the type of signal it carries and the direction of propagation. First, the 145.500 MHz RF signal is generated by a Kenwood TH-D7(G) ham radio. This signal is sent to a video gate that breaks the continuous tone into pulses. The gate is controlled by pulses sent from the pulser. The pulses sent to the gate are delayed by 6μs to allow the timing pulse to reach the oscilloscope at nearly the same time as the RF pulse. Simultaneously, a timing signal is sent to a line driver. The line driver is a modified differential amplifier and is able to transmit the pulse across 3500 feet of 24 gauge twisted pair cable. At the other end of the twisted pair the timing signal is reconstructed by a line receiver and a digital discriminator. For accuracy, it is necessary to have as sharp a rise time as possible on the timing pulse. The RF pulse is passed through a preamplifier and a linear amplifier on the receiving end. Both signals are collected by a digital oscilloscope for comparison. In summary, there are three pulses: one is the radio pulse transmitted through the salt, and the other two are the TTL pulses that simultaneously control the gate and provide the timing baseline for the radio pulse.

The accuracy conditions are determined as follows. The index of refraction is $n = \frac{c}{v}$ where $v = \frac{d}{t}$. In general,

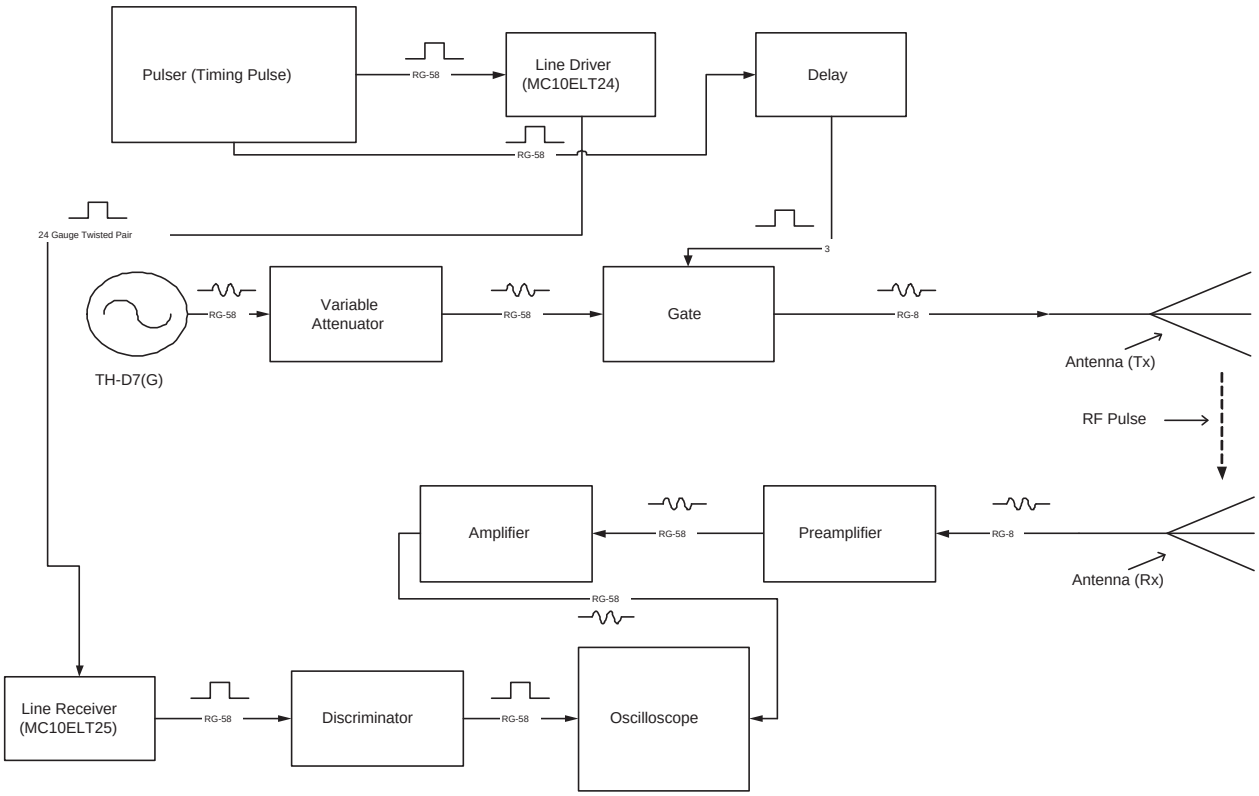

Fig. 2.1: System Diagram

uncertainties are propagated by

$$\Delta Z = Z\sqrt{\sum_{i=1}^{N}\left(\frac{\Delta X_i}{X_i}\right)^2} \tag{2.1}$$

where ΔZ is the desired uncertainty, Z is the parameter of interest, ΔX_i are the uncertainties of the known parameters X_i. Inserting the expression for the index of refraction and the velocity of light with a medium, Equation 2.3 becomes

$$\Delta n = n\sqrt{\left(\frac{\Delta d}{d}\right)^2 + \left(\frac{\Delta t}{t}\right)^2}. \tag{2.2}$$

Assuming $d = 300$ m, $\Delta d = 0.01$ m, $n = 2.45$, $\Delta t = 40$ ns, and $t = 2.5 \cdot 10^{-6}$ sec, $\Delta n = 0.039$. This says that for the largest rise time (~ 40 ns from the discriminator), the uncertainty on the index of refraction will be about 0.04, or 2%.

2.3 Component Specifications

2.3.1 Gate

The gate (Figure 2.2) is built around an OPA 693 video switch. It was originally designed for high speed switching between video feeds and is rated for frequencies up to 700 MHz. External inputs are ±5 V power and a +5 V disable pulse. The continuous 150 MHz signal is sent to the non-inverting input. The inverting input is tied to ground. When the disable pin is high (TTL ON) the gate is open and the signal can pass unimpeded. When the pin is low the gate is closed. The gate can open within 25 ns and close within 3 μs. The rise time was the reason this particular chip was chosen as shorter rise times allow for more accurate timing measurements.

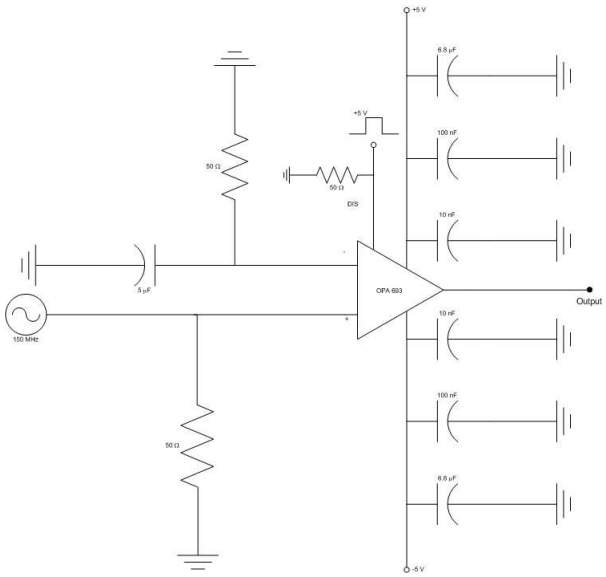

Fig. 2.2: Gate Diagram

The gate can handle input signals of 5 Volts, peak-to-peak value. The lowest setting on the TH-D7 was 0.5 Watt. Transmitted across 50Ω RG-58, the signal had a root-mean-square voltage of 5 Volts. This meant the peak-to-peak voltage was a factor of $\sqrt{2}$ higher. To pull this below 5 Volts peak-to-peak, a variable attenuator was placed between the radio and the gate and set for 3 decibels. This was calculated from

$$dB = 20 \log \left(\frac{V_f}{V_i} \right). \tag{2.3}$$

Running the gate without the attenuation produced spurious signals around 20 MHz. These signals caused distortions in the transmitted RF pulse (Figure 2.3(a)). While seeming nothing more than a nuisance, these signals were actually transmitted and could be received, causing harmful interference to other stations. A spurious signal

meant that some of the power was going into useless frequencies. Attenuating the input to the gate solved the problem. Figure 2.3(b) shows the gate output with 4 dB of attenuation on the input.

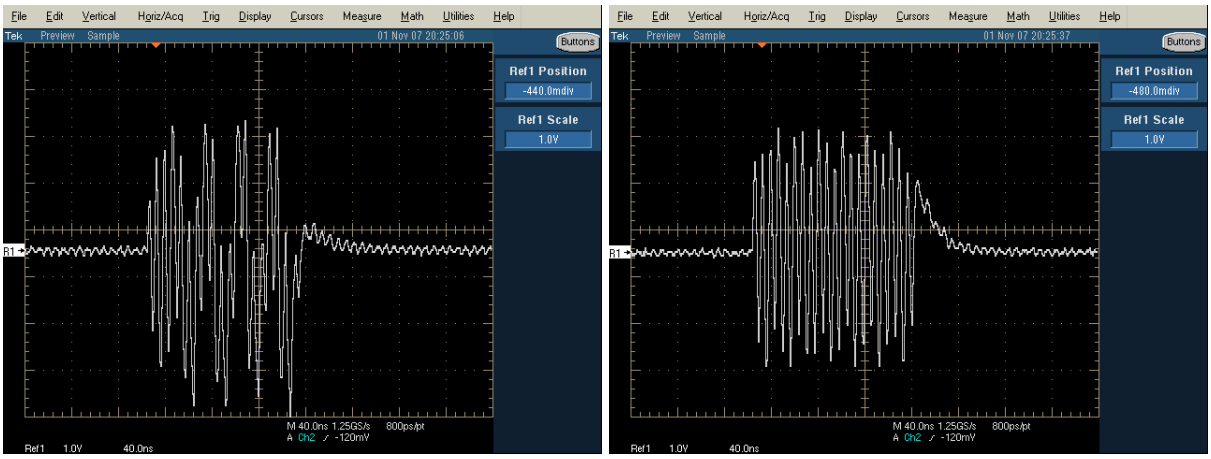

(a) No Attenutation (b) 4 dB Attenuation

Fig. 2.3: Gate Output with and without Attenuation

2.3.2 Line Transmission System

The line transmission system (Figure 2.4) includes the line driver and receiver. This system was needed to transmit the timing pulse across the cable length needed for a long distance test. The first half of the system is the line driver module. This is composed of a TTL to differential ECL converter (MC10ELT24) and a driver/receiver dual package chip (MC10HEP16). For the front end only the driver half was used. The ELT24 takes a standard TTL pulse, in this case generated by the pulser, and converts it to a differential ECL pulse. The ECL pulse is then sent to the line driver (MC10HEP16) for transmission. The transmission line is 24 gauge twisted pair, each strand of which is terminated to -2V across a 150Ω resistor.

The receiver module works like the transmitter in reverse. The signal cable is once again terminated upon entering the circuit. In this case, the receiver half of the HEP16 is used and the outputs sent to the ECL-TTL converter half of another ELT24. After leaving the receiver module the signal is further cleaned by a discriminator to give a rise time on the order of about 40 nanoseconds, or $\Delta n = 0.039$.

The testing of the line transmitter was conducted in stages. First, it was necessary to establish that the pulser was actually sending the desired pulse. A short piece of RG-58 coaxial cable was attached between the positive pulser output and the oscilloscope. The result is shown in Figure 2.5. Next, the pulser was connected to the line driver module, twisted pair, and line receiver module. The signal was then allowed to propagate across to the far end. (Figure 2.6)

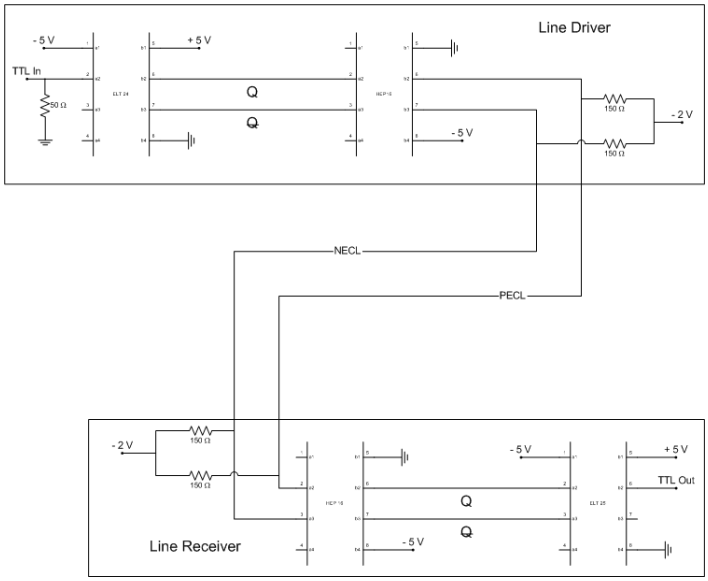

Fig. 2.4: Line Transmission System

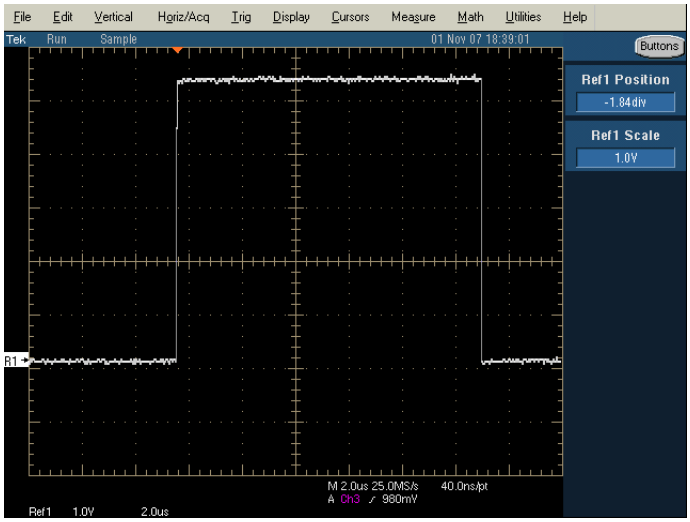

Fig. 2.5: Positive Pulser Output

As can be seen, the pulse has much less amplitude and has a slightly messier leading edge than the original, but is still distinctly recognizable. The discriminator placed after the line receiver module was able to clean the signal and produce a rise time of about 40 nanoseconds. (Figure 2.7) The discriminator pulse is significantly shorter than the original pulser output, but the leading edge is the only part of interest.

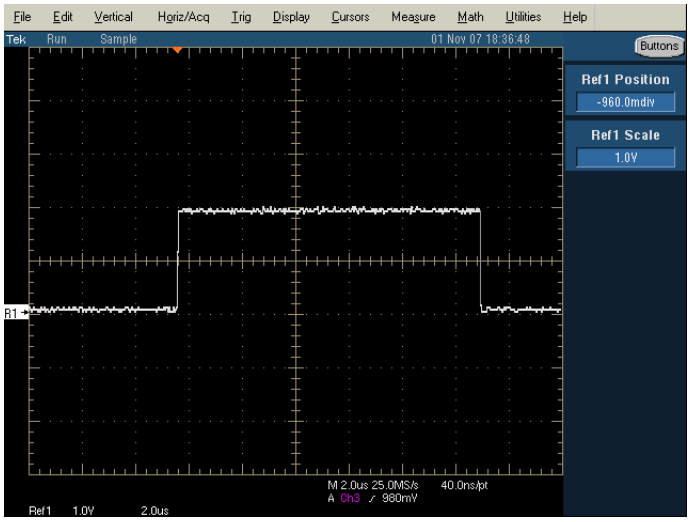

Fig. 2.6: Line Transmission Output

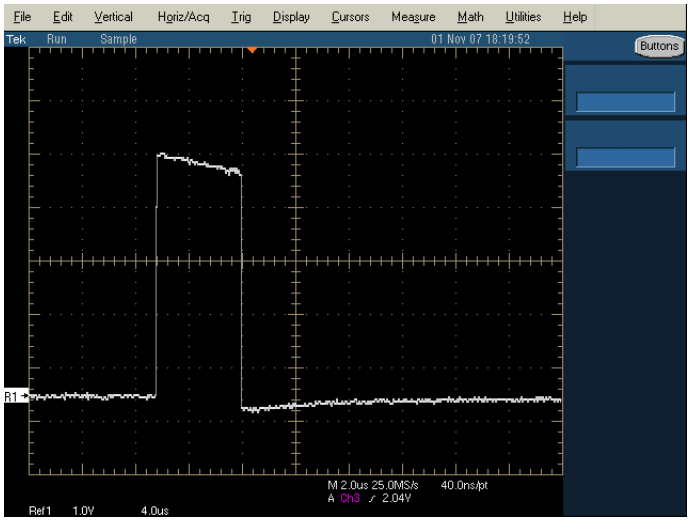

Fig. 2.7: Fully Reconstructed Trigger/Timing Pulse

2.3.3 Preamplifier

Because of the small size of the received signal and large external RF background noise outdoors, it was necessary to construct a preamplifier. A preamplifier is the component of a radio that allows one to pick a single station out of the cacophony of background noise. It is composed of a bandpass filter followed by an amplifier. The preamplifier (Figure 2.8) was copied from the 1972 edition of the ARRL Handbook.[26] In the mines, there is virtually no RF background, but for testing in the lab and outdoors any RF will be seen by the oscilloscope and will interfere with the desired signal. The filter portion of the preamp eliminates the background and the amplifier

portion raises the level of the remaining signal.

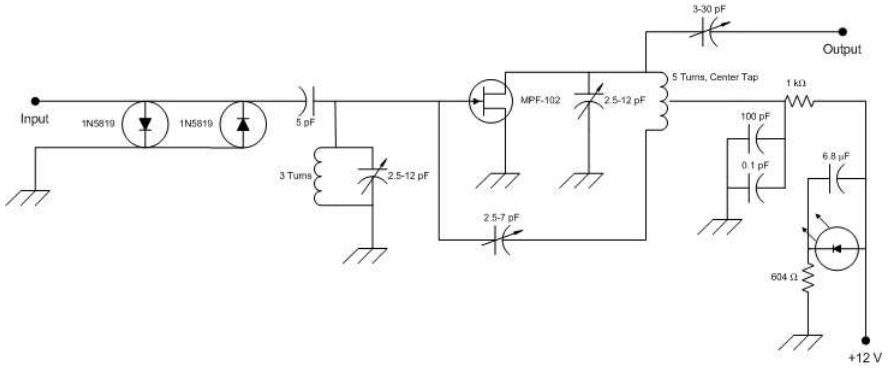

Fig. 2.8: The Preamplifier

After careful construction and tuning, the preamp was found to filter most of the noise and have a gain of 7.6 dB. (See Figures 2.9(b) & 2.9(a) and Equation 2.3.)

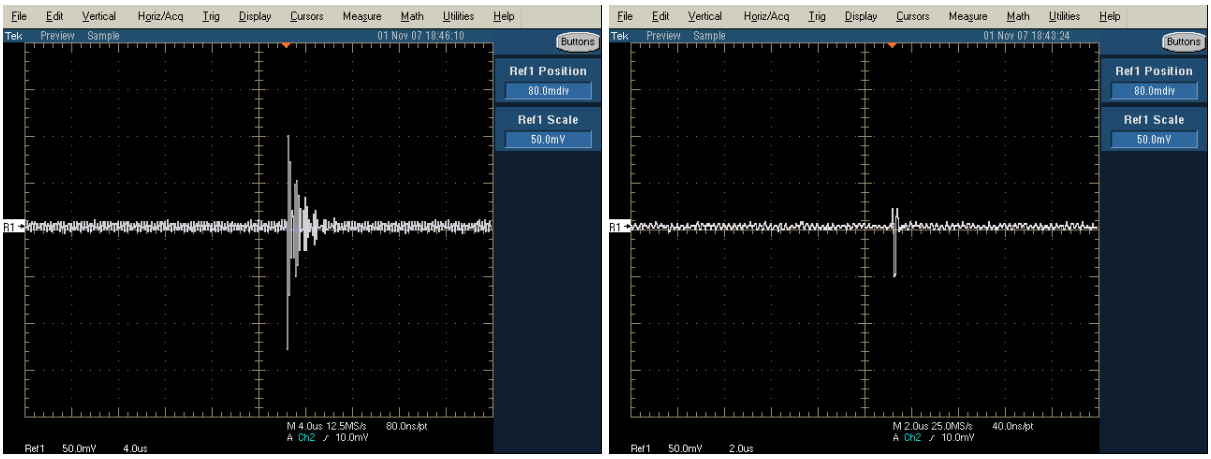

(a) Output of Preamplifier

(b) Input to Preamplifier

Fig. 2.9: Output and Input of Preamplifier

2.3.4 Linear Amplifier

The signal from the preamp was then passed to a linear amplifier for final amplification. The linear amplifier had an advertised gain of 20 dB for input signals below +11 dBm, or 12 mW. The 50Ω cables limited the maximum voltage for the input signals to 0.77 Volts. This limit was never a problem since none of the signals from the preamp were ever larger than 0.2-0.3 V. The output signal shown in Figure 2.10 gives a maximum voltage of 1.8 Volts with the bulk of the signal around 800 mV. That together with the 120 mV from the preamp gives a gain of 23 dB, showing that the linear amplifier was working as advertised.

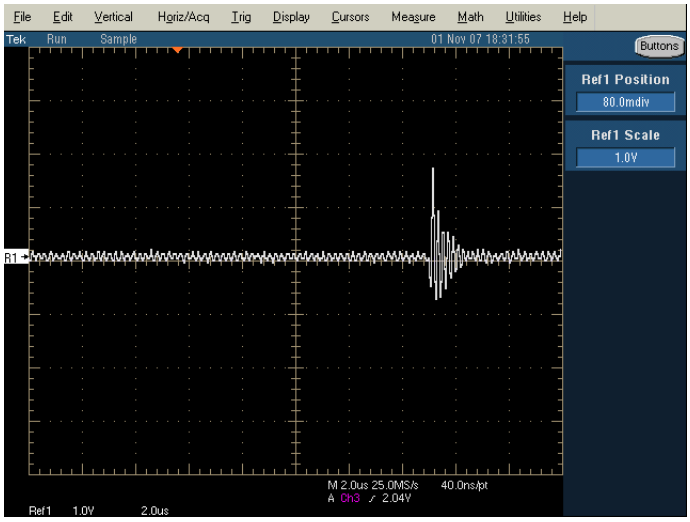

Fig. 2.10: Output of Linear Amplifer

2.3.5 Antennae

Seemingly the simplest part of the system, the antennae are actually two of the most critical. If the antennae are not tuned and constructed correctly, the signal losses will kill the experiment. An antenna is considered tuned when its radiation resistance matches the characteristic impedance of the cable driving it. Impedance mismatches cause standing waves in the antenna and cables, reducing the efficiency and amount of power transmitted. At higher power impedance mismatches can cause dangerous reflections in the transmission line. Accurately tuned antennae will transmit nearly all of the power sent through them while poorly tuned antennae will reflect most of the power back down the cable. The antennae were constructed from scratch using 0.75 inch copper pipe and brass rods. As seen in Figure 2.11, the antennae are sheathed in PVC to protect them from the mine environment and to provide stuctural stability. The signal is carried in along a piece of RG-174 coaxial cable which is fed through the center of the copper pipe. At the BNC, the ground sheath of the cable is soldered to the pipe and the center wire is connected to the brass rod via the center of the BNC. The ends are capped and the whole thing will fit inside of a two inch diameter bore hole.

The design chosen was a half wave center driven dipole antenna. This type of antenna emits the majority of its power in a plane perpendicular to the antenna. The radiated power per unit solid angle of an ideal (no losses) dipole antenna is given by

$$\left\langle \frac{dP}{d\Omega} \right\rangle = \frac{I_0^2}{2\pi v} \left(\frac{\cos\left(\frac{m\pi}{2}\cos\theta\right) - \cos\left(\frac{m\pi}{2}\right)}{\sin\theta} \right)^2 \quad [16] \tag{2.4}$$

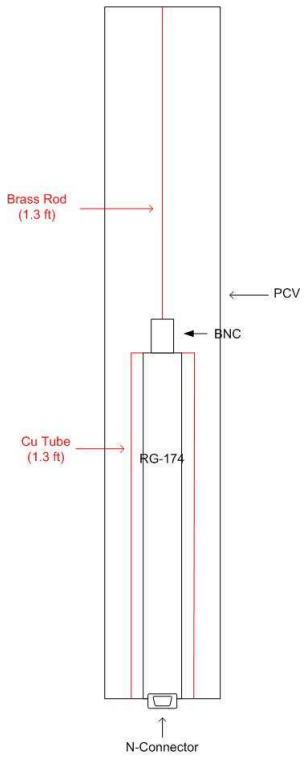

Fig. 2.11: Antenna Schematic

where m denotes harmonic number, v the velocity of the electromagnetic wave in the medium, and θ the spherical altitude angle. For a half wave antenna $m = 1$, reducing Equation 2.4 to

$$\left\langle \frac{dP}{d\Omega} \right\rangle_{m=1} = \frac{I_0^2}{2\pi v} \frac{\cos^2\left(\frac{\pi}{2}\cos\theta\right)}{\sin^2\theta}. \quad [16] \tag{2.5}$$

Plotting Equation 2.5 shows that the majority of the power is transmitted into the plane orthogonal to the center of the antenna. Accounting for losses only decreases the size of the lobes but does not change their shapes.

The antennae were tested by transmitting a pulse and looking for it on the oscilloscope. Since they were tuned for $\sim$ 150 MHz most of the RF energy should have been transmitted, but a test was necessary to ensure proper functioning. Figure 2.9(b) shows the signal received by the second antenna after being transmitted by the first. The receiving antenna was connected directly to the oscilloscope. As is seen, both antennae function, even if the signal is rather small.

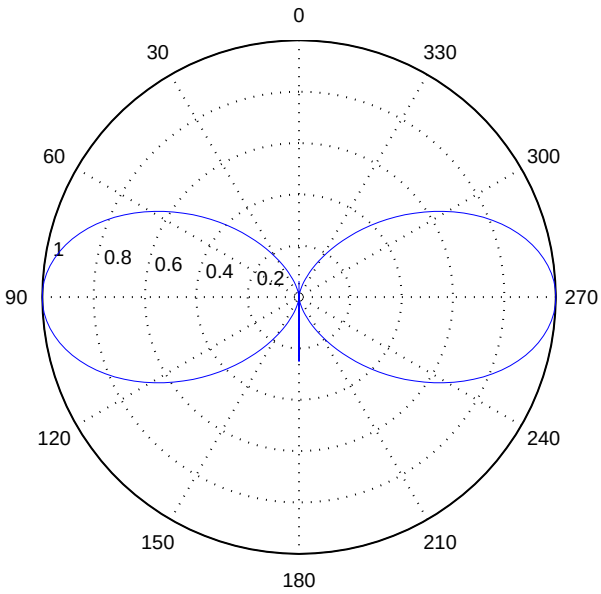

Fig. 2.12: Radiation Pattern for a Half Wave Dipole

2.4 Outdoor Testing

Once it was shown that the system functioned inside the lab, the next step was to take it outside to try it in the open. This had the double effects of isolating the transmitter and receiver from the reflective elements in the lab and trying the system under semi-hostile conditions. As shown in Figure 2.10, the received signal at 15 feet in the lab averaged $\sim$ 700 mV. Without outdoor testing it was impossible to know if the reflections from the lab would hurt, help, or leave the signal unchanged. Also, transporting and assembling the system in the field would expose problems with durability and organization.

The site chosen for the test was the LSU Quadrangle. This had the advantages of being relatively close to the lab and having accessible AC power. This made it easy to transport the equipment, convenient to make repairs when necessary, and power the system without the need for batteries and DC-AC inverters. The Quadrangle was several hundred feet wide and several hundred more in length, leaving plenty of room for long range testing. Both of the antennae were held so that they were perpendicular to the ground and parallel to each other. They were also placed at least 30 feet from walls to minimize the contributions of reflections. For convenience, the transmitting end was placed on a cart and moved to different positions while the receiving station was stationary.

The objective was to make two types of measurements. First, the received signal would be measured at various distances with the gate in place to ensure long range index of refraction measurements were feasible. Power

is proportional to the square of the voltage and the inverse square of the distance, so plotting the received voltage versus distance should give a linear slope. The second measurement was to attempt to calculate the speed of light through air from the timing data. The third was a simple attenuation test. The first measurements were made at a distance of 30 feet. Figure 2.13(a) shows that the received signal was not as large as expected.

As can be seen, the received signal is only about 70 mV, much smaller than what was observed in the lab. There was also a 20 mV background. The next measurements were made at 90 feet. At that point the signal is only a few mV and barely distiguishable from the noise (Figure 2.13(b)). It was immediately apparent that there simply was not enough power being transmitted to enable detection of a signal in this manner.

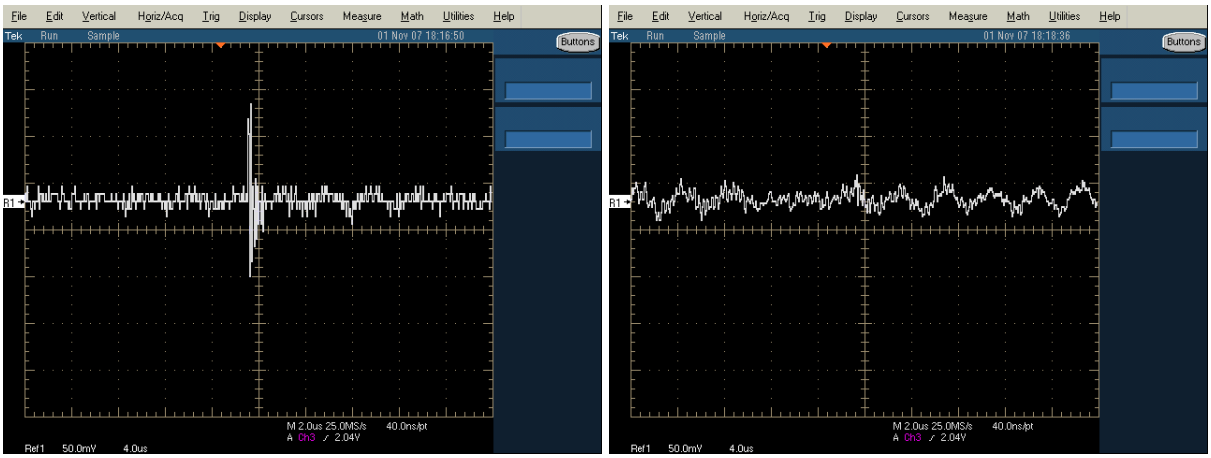

(a) Received Signal at 30’ (b) Received Signal at 90’

Fig. 2.13: Signals at 30’ and 90’

3. CONCLUSIONS

3.1 Experiment Results

The results of this period of experimentation indicate that although the system does function at short range, there is not enough power being transmitted. Calculations suggest that at 90 feet there should be an 80 mV signal. Assuming a 100% efficient antenna, all of the power will be radiated. From Figure 2.3(b) it is seen that the output voltage is about 5 Volts, peak to peak. This translates to a RMS voltage of 3.54 Volts. Power is defined as $P = \frac{V^2}{R}$, so with a 50 Ω cable, $P = 0.25$ Watt. A dipole antenna has an effective cross section approximately the square of the length of an element. The antennae were approximately a meter long giving and cross section of approximately 0.25 m^2. At 90 feet, the intensity of the signal should have been $7.20 \cdot 10^{-4}$ W/m^2. Multiplying by the antenna cross section gives that the received power should be $1.8 \cdot 10^{-4}$ Watt. This translates to an induced potential along the antenna of 95 mV, far below what was seen. This indicates that there are unknown factors causing significant signal loss. The signal is still present, so it might be possible to circumvent the problem by boosting the power. It was also shown how environmental factors can seriously affect radio transmissions at these frequencies. These environmental factors include everything from background noise to the metal used in the walls of the lab. Inside the lab the received signals were almost a Volt. Outside, they were barely visible. With virtually no signal, the other portions of the experiment were unable to be completed.

3.2 Future Plans

Since the system does work, it would be senseless to abandon it yet. What is needed is to find the source of power loss. The cables have been checked for continuity, but it would make sense to check again. The two most likely sources of attenuation are the gate and the preamp. The gate has been checked and have been stable; however, the preamp has had problems with stability in the past. If the preamp is tuned poorly it can begin oscillating and generating a signal on its own. This was not observed during the test, but should be made note of for future testing. Also, if the preamp is not tuned properly the pass band may be too far away from the signal frequency. In that case the preamp would actually block most of the desired signal.

It might also be possible to increase the transmitted power and solve the problem through brute force. The biggest limitation on power is the threshold of the OPA 693. One possibility is simply to find a more durable gate. This would require redesigning and reconstructing the gate module but would allow the radio to be run at higher power. The TH-D7 can deliver up to 5 Watts, which has a peak to peak voltage of ~ 22 Volts. This would be a ten-fold increase in power, corresponding to a four-fold increase in range. Another option is to invest in a power amplifier. Power amplifiers can be made to deliver thousands of Watts. This is far too much, but smaller models putting out 50 Watts are available. Attaching a power amplifier after the gate would avoid the need to rebuild the gate. The problem would then become the linear amplifier on the receiving end. The linear amplifier can only handle 0.77 Volts on the input, so care would have to be taken to prevent burning it out. If these problems can be resolved then the system will be able to function as desired.

3.3 Closing Remarks

The SalSA Experiment will provide interesting new data for the field of neutrino astrophysics. The series of new detectors that will be coming on line in the next few years practically guarantee the detection of UHE neutrinos. With the recent Auger results clearly showing the GZK cutoff is real, the UHE neutrinos must exist, and it will be the job of the next generation of neutrino detectors to find them. The information they carry is invaluable to the astrophysical community. SalSA will be in the forefront of new discoveries about the universe. However, before this can happen a site must be chosen. The approach presented in this paper has the potential to allow teams to enter potential sites and take the measurements with a minimum of complication. Despite the problems encountered, taking the steps outlined will make it work. Once a site has been chosen, the SalSA collaboration will be able to begin testing protypes and eventually build a full scale detector.

BIBLIOGRAPHY

[1] G. Askaryan. Excess negative charge of an electron-photon shower and its coherent radio emission. *JETP*, 14(2), February 1962.

[2] B.W. Carroll and D.A. Ostlie. *Modern Astrophysics*, chapter 26, pages 1157–1214. Addison-Wesley Publishing Company, Inc., 1996.

[3] M.L. Cherry. Site studies for a high energy underground neutrino telescope in a Louisiana salt mine. SalSA Research Proposal.

[4] M.L. Cherry. Cosmic neutrino fluxes – scaling from UHE gamma rays. In *Arkansas Gamma-Ray and Neutrino Workshop – 1989*, 1990.

[5] The Pierre Auger Collaboration. Correlation of the highest-energy cosmic rays with nearby extragalactic objects. *Science*, 318, November 2007.

[6] E. Andrès et. al. Observation of high-energy neutrinos using Čerênkov detectors embedded deep in Antarctic ice. *Nature*, 410(441), March 2001.

[7] H. Hanada et. al. A highly sensitive optical detector for a use in deep underwater. Preprint submitted to Elsevier Preprint, December 1996.

[8] J. Adams et. al. The radio ice cherenkov experiment. In *Proceedings of the 4th Tropical Workshop on Particle Physics and Cosmology*, 2003.

[9] J. Ahrens et. al. Limits on diffuse fluxes of high energy extraterrestrial neutrinos with the AMANDA-B10 detector. *Physical Review Letters*, 90(251101), June 2003.

[10] L.K. Resvanis et al. Recent results from NESTOR. In *Neutrino Oscillations in Venice*, 2006.

[11] A. Goldschmidt. The IceCube detector. In *Proceedings of the 24th International Cosmic Ray Conference*, 2001.

[12] P.W. Gorham, D. Saltzberg, R.C. Field, E. Guillian, R. Milinčić P. Miočinović, D. Walz, and D. Williams. Accelerator measurements of the Askaryan effect in rock salt: A roadmap toward teraton underground neutrino detectors. *Physical Review D*, 72(023002), April 2005.

[13] K. Greisen. End to the cosmic-ray spectrum? *Physical Review Letters*, 16(17), April 1966.

[14] IceCube Team. IceCube in depth. Internet Source: http://www.icecube.wisc.edu/. IceCube project home page.

[15] J.D. Jackson. *Classical Electrodynamics*, chapter 13, pages 637–640. John Wiley & Sons, Inc., Third edition, 1999.

[16] J.B. Marion. *Classical Electromagnetic Radiation*, chapter 8, pages 242–251. Academic Press, 1965.

[17] D.H. Perkins. *Introduction to High Energy Physics*, chapter 2, pages 57–61. Addison-Wesley Publishing Company, Inc., Third edition, 1990.

[18] K. Reil. SalSA: A teraton UHE neutrino detector. In *Proceedings of the Particles and Nuclei International Conference*, 2005.

[19] L.K. Resvanis. High energy neutrino telescopes. *Nuclear Physics B (Proc. Suppl.)*, 122(000024), 2003.

[20] P. Sokolsky. *Introduction to Ultrahigh Energy Cosmic Ray Physics*, volume 76 of *Frontiers in Physics*, chapter 2, pages 4–17. Addison-Wesley Publishing Company, Inc., 1989.

[21] Robert Svoboda. Experimental status of high energy neutrino astronomy. In *Arkansas Gamma-Ray and Neutrino Workshop – 1989*, 1990.

[22] AMANDA Team. AMANDA II project. Internet source: http://amanda.uci.edu/. AMANDA project home page.

[23] ANTARES Team. Overview of the ANTARES experiment. Internet Source: http://antares.in2p3.fr/Overview/index.html. ANTARES project home page.

[24] DUMAND Team. DUMAND at the University of Hawaii. Internet Source: http://www.phys.hawaii.edu/∼dumand/. DUMAND project home page.

[25] NESTOR Team. NESTOR Institute for Astroparticle Physics. Internet Source: http://www.nestor.org.gr/. NESTOR project home page.

[26] E.P. Tilton and D.A Blakeslee, editors. *The Radio Amateur's VHF Manual: A Manual of Amateur Radio Communication on the Frequencies Above 50 Megahertz*, chapter 4, page 55. American Radio Relay League, third edition, 1972.

[27] G.T. Zatsepin and V.A. Kuz'min. Upper limit of the spectrum of cosmic rays. *JETP Letters*, 4(3), August 1966.

VITA

The author was born in 1983 in Beaufort, South Carolina. He spent the first fifteen years of his life as a military dependent. Consequently he has lived in places ranging from San Diego, California, to Dunoon, Scotland. The author began school in Scotland. He graduated from Northshore High School in Slidell, Louisiana, in 2001 and then enrolled at Louisiana State University. Upon completing a Bachelor of Science in physics, he was accepted into the Louisiana State University graduate program in physics. The author will soon be transferring to Mississippi State University to complete doctoral work in physics.